

Nature of Charge Carrier Recombination in CuWO₄ Photoanodes for Photoelectrochemical Water Splitting

Ivan Grigioni,* Annalisa Polo, Chiara Nomellini, Laura Vigni, Alessandro Poma, Maria Vittoria Dozzi, and Elena Selli



Cite This: *ACS Appl. Energy Mater.* 2023, 6, 10020–10029



Read Online

ACCESS |



Metrics & More



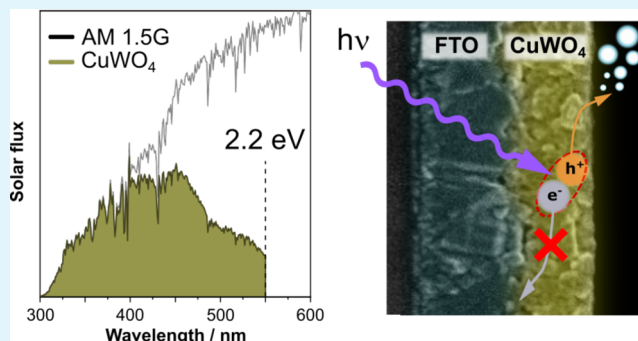
Article Recommendations



Supporting Information

ABSTRACT: CuWO₄ is a ternary semiconductor oxide with excellent visible light harvesting properties up to 550 nm and stability at high pH values, which make it a suitable material to build photoanodes for solar light conversion to hydrogen via water splitting. In this work, we studied the photoelectrochemical (PEC) performance of transparent CuWO₄ electrodes with tunable light absorption and thickness, aiming at identifying the intrinsic bottlenecks of photogenerated charge carriers in this semiconductor. We found that electrodes with optimal CuWO₄ thickness exhibit visible light activity due to the absorption of long-wavelength photons and a balanced electron and hole extraction from the oxide. The PEC performance of CuWO₄ is light-intensity-dependent, with charge recombination increasing with light intensity and most photogenerated charge carriers recombining in bulk sites, as demonstrated by PEC tests performed in the presence of sacrificial agents or cocatalysts. The best-performing 580 nm thick CuWO₄ electrode delivers a photocurrent of 0.37 mA cm⁻² at 1.23 V_{SHE} with a 7% absorbed photon to current efficiency over the CuWO₄ absorption spectrum.

KEYWORDS: photoelectrocatalysis, ternary oxides, solar water splitting, solar light, renewable energy



1. INTRODUCTION

Photoelectrochemical (PEC) water splitting produces clean O₂ and H₂ from water by exploiting sunlight directly.¹ The oxygen evolution reaction requires anodic semiconductor materials that are resistant to harsh reaction conditions. Moreover, an ideal material needs a narrow band gap to absorb a considerable portion of visible light and guarantee a solar to hydrogen efficiency above 10%, which is the lower limit for industrialization.^{2,3}

Binary metal oxide-based photoelectrodes, such as WO₃ and α -Fe₂O₃,^{4,5} initially attracted interest as visible-light-active materials. WO₃ has a high electron diffusion length and mobility,^{4,6–8} and optimized electrodes allow almost complete absorbed photons to current conversion efficiency. However, WO₃ has poor chemical stability in neutral or basic pH and a relatively wide band gap (2.6–2.7 eV). On the other hand, hematite (Fe₂O₃) has an intriguing narrow band gap of 2.0 eV with potential solar to hydrogen conversion efficiency (η_{SHE}) up to 15% (Table 1),⁹ but limited charge carrier lifetime (below 1 ns in undoped Fe₂O₃)^{10,11} and mobility, which translate into suboptimal PEC performances.

More recently, ternary oxides such as BiVO₄ with an intermediate band gap of 2.4 eV emerged as highly efficient materials for photoelectrocatalytic applications.^{12–16} State-of-the-art BiVO₄ photoanodes show close-to-unity incident photon

Table 1. Commonly Used Semiconductor Oxide Photoanodes

semiconductor	BG ^a /eV	J _{max} ^b /mA cm ⁻²	η_{SHE} ^c
WO ₃	2.6	4	5%
BiVO ₄	2.4	7	8%
CuWO ₄	2.2	10	12.5%
Fe ₂ O ₃	2.0	12.5	15%
CuMoWO ₄	2.0	12.5	15%

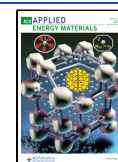
^aband gap (BG). ^bmaximum current density (J_{max}). ^csolar to hydrogen efficiency (η_{SHE}) of semiconductor photoanodes assembled in a two-electrode tandem PEC cell, assuming complete light absorption and conversion of photons with energy larger than the band gap and 100% faradaic efficiency to H₂ and O₂.

to current efficiency up to 480 nm.¹⁷ However, the band gap of BiVO₄ is slightly larger than that desired for optimal photoanode materials. Indeed, a charge carrier recombination-free BiVO₄

Received: June 28, 2023

Accepted: September 1, 2023

Published: September 20, 2023



electrode (i.e., with an incident photon to current efficiency close to 100% up to the absorption onset at 520 nm) would lead to only 7–8% solar energy to hydrogen conversion, which implies that BiVO₄ should be used in combination with narrower band gap materials in complex multilayer photoanodes.¹⁸

Ternary CuWO₄ oxide has a band gap of 2.2 eV, and it could achieve an η_{SHE} of 12.5%.¹⁹ Furthermore, the CuWO₄ band gap can be narrowed by substituting tungsten with molybdenum in quaternary CuW_xMo_yO₄. For example, CuW_{0.5}Mo_{0.5}O₄ has a band gap of 2.0 eV, corresponding to an absorption edge of 650 nm.^{20–22} This tungstate family is stable in neutral and slightly basic pH because of the overlap between Cu 3d orbitals with O 2p orbitals.^{23,24} This hybridization is also responsible for the negative shift of the CuWO₄ valence band compared to that of binary WO₃.²⁵ Moreover, CuWO₄ is suitable to assemble heterojunction systems with BiVO₄,^{26,27} likewise WO₃.^{28–32}

In prior studies, we investigated the charge carrier dynamics in transparent CuWO₄ electrodes and found that charge carriers mostly recombine within a 10 ps time scale, with only ca. 10% of them surviving longer than 1 ns to potentially run water oxidation.³³ In this work, we sought to experimentally study the intrinsic limits that hamper CuWO₄ photoactivity by employing a suite of PEC experiments to understand the factors shaping its performance. We prepared a series of thin-film CuWO₄ electrodes through a citrate-based aqueous solution method and tuned the CuWO₄ thickness to increase visible light exploitation of the photoanodes. To seek information on the charge carrier recombination processes occurring in bulk and surface CuWO₄ and on their implication in the overall PEC performance, we tested the electrodes under front- and back-side irradiation in both simulated solar light and monochromatic irradiation experiments. We also varied the light intensity to study the effect of the charge carrier density on the PEC activity and found that the PEC performance of CuWO₄ is light-intensity-dependent, with charge recombination increasing with light intensity, and that most photoproduced charge carriers recombine in bulk sites.

2. EXPERIMENTAL SECTION

2.1. Materials. The following chemicals were employed in the present work: copper(II) nitrate trihydrate (99% purity, Sigma-Aldrich), ammonium metatungstate hydrate (NH₄)₆H₂W₁₂O₄₀·xH₂O (99% purity, Fluka), citric acid (99% purity, Sigma-Aldrich), deionized water, boric acid (99.5% purity, Sigma-Aldrich), and KOH (99.5% purity, Sigma-Aldrich). All chemicals were used as received, with no further purification.

2.2. Photoelectrodes Preparation. The CuWO₄ thin films were prepared following a previously reported procedure.³³ Specifically, a 0.5 M solution of CuWO₄ was prepared by dissolving 14 mmol of citric acid in 5.3 mL of ethanol and 2.4 mL of deionized H₂O, followed by the addition of 5 mmol of Cu(NO₃)₂·3H₂O under vigorous stirring and a stoichiometric amount of ammonium metatungstate hydrate. Fluorine-doped tin oxide (FTO) glass (Pilkington Glass, TEC-7, thickness of 2 mm) was used as conductive glass to prepare the FTO/CuWO₄ electrodes. The FTO glass was cleaned under sonication for 30 min in a soap-water solution, rinsed thoroughly with water, sonicated for 30 min in ethanol, and then dried in air. After cleaning, the electrodes were prepared by spin coating 100 μ L of the CuWO₄ solution on FTO, at 4000 rpm for 30 s. Then, the CuWO₄ film was preannealed at 250 °C for 10 min and then annealed at 550 °C for 1 h. Prior to any test, the photoanodes were treated for about 30 s in a 0.5 M HCl aqueous solution to eventually eliminate any trace of CuO, then washed with distilled water and dried in air. The deposition, annealing, and HCl

cleaning steps were repeated up to six times to prepare multilayer electrodes with the desired thickness and light absorption properties.

The NiFeO_x cocatalyst was deposited onto the photoelectrodes employing a hydrothermal method,³⁴ by soaking the CuWO₄ electrode into an aqueous solution containing NiCl₂ (0.2 mM) and FeCl₃ (29.8 mM) as Ni²⁺ and Fe³⁺ sources in a closed vessel for 45 min at 100 °C.

2.3. Optical, Morphological, Structural, and Photoelectrochemical Tests. The absorption spectra of the CuWO₄ thin films on the electrodes were recorded in transmission mode with a Jasco V-650 spectrophotometer. The crystalline phase of the photoactive materials was determined by XRD analysis of the deposited thin films, using a Philips PW 1830/40 X-ray powder diffractometer equipped with a Cu tube at 40 kV and 40 mA. Top-view and cross-sectional field emission scanning electron microscopy (FESEM) images were acquired employing a LEO 1430 scanning electron microscope operating at a 10 kV accelerating voltage and an 8 mm working distance.

PEC measurements were performed using a homemade cell and an Autolab PGSTAT 12 potentiostat controlled by the NOVA software. In a typical setup, the electrode was used as the working electrode, a Pt wire was used as the counter electrode, and Ag/AgCl (3.0 M in NaCl) was used as the reference electrode. The photoanodes were tested under both back-side irradiation (through the FTO/CuWO₄ interface) and front-side irradiation (through the CuWO₄/FTO interface). The light source was an Oriel, Model 81172 Solar Simulator equipped with an AM 1.5 G filter. In simulated solar light irradiation experiments, the light intensity was measured with a Thorlab PM200 power meter equipped with a Si power head (S130VC) and set at 100 mW cm⁻² (1 sun). In PEC experiments under simulated solar light with different intensities, a neutral light attenuator filter was employed to obtain 25 and 50 mW cm⁻² intensities (0.25 and 0.5 sun, respectively) and a quartz lens was used to increase the intensity to 150 and 200 mW cm⁻² (1.5 and 2 suns, respectively).

PEC experiments were carried out in a 0.1 M potassium borate (KBi) buffer solution at pH 9 unless otherwise stated. The potential vs Ag/AgCl was converted into the standard hydrogen electrode (SHE) scale using the following equation

$$E_{\text{SHE}} = E_{\text{Ag/AgCl}} + 0.059 \text{ pH} + E^{\circ}_{\text{Ag/AgCl}}$$

$$\text{, with } E^{\circ}_{\text{Ag/AgCl}} (3.0 \text{ M NaCl})$$

$$= 0.210 \text{ V at } 25^{\circ}\text{C}$$

The incident photon-to-current efficiency (IPCE) was measured using a 300 W Lot-Oriel Xe lamp equipped with a Lot-Oriel Omni- λ 150 monochromator and a Thorlabs SC10 automatic shutter. A 1.23 V bias vs SHE (V_{SHE}) was applied, and the current was measured with a 10 nm step within the 350 to 600 nm wavelength range. The incident light power was measured at each wavelength by using a calibrated Thorlabs S130VC photodiode connected to a Thorlabs PM200 power meter. The IPCE at each wavelength was calculated using the following equation

$$\text{IPCE}_{\lambda} = \frac{1240 \times J_{\lambda}}{P_{\lambda} \times \lambda} \times 100$$

where J_{λ} is the photocurrent density (mA cm⁻²) and P_{λ} (mW cm⁻²) is the power of the monochromatic light at wavelength λ (nm).

The internal quantum efficiency (IQE) at each wavelength was calculated by combining the IPCE curve with the absorption (A) spectrum of each photoanode

$$\text{IQE}_{\lambda} = \frac{\text{IPCE}_{\lambda}}{(1 - 10^{-A_{\lambda}})}$$

3. RESULTS

3.1. Characterization of CuWO₄ Multilayer Photoanodes. We started by studying the morphology of the CuWO₄ photoanodes by field emission scanning electron microscopy (FESEM). Top-view images (Figure 1A,B) reveal

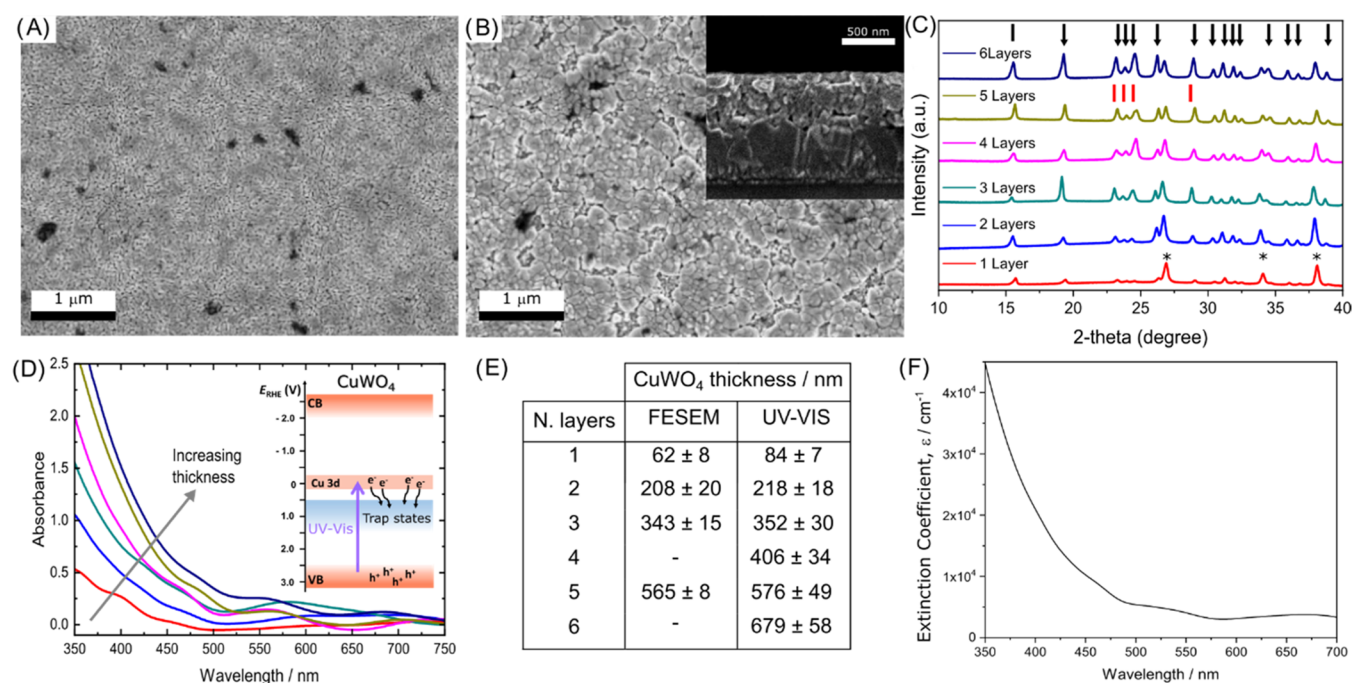


Figure 1. Field emission scanning electron microscopy (FESEM) top views of (A) 2 layers and (B) 5 layers of CuWO₄. Inset in (B): cross section of the CuWO₄ film obtained by depositing 5 layers. (C) XRD patterns of the CuWO₄ electrodes. The diffraction signals of WO₃ (JCPDF 89-4476), CuWO₄, and underlying FTO are identified with red bars, black arrows, and asterisks, respectively. (D) Absorption spectra of the CuWO₄ photoanodes with increasing semiconductor thickness. Inset: scheme of the optical transitions in CuWO₄. (E) Thickness of the electrodes with 1–6 CuWO₄ layers, from cross-sectional FESEM images (left column) and calculated from the absorption coefficient at 420 nm (right column). (F) Extinction coefficient vs wavelength of a 5-layered CuWO₄ electrode.

that CuWO₄ progressively covers the FTO substrate uniformly. Two deposited layers provide a continuous coating film consisting of oval-shaped nanostructures (Figure S1 in the Supporting Information). Bigger grains form in thicker electrodes (Figure 1B).

Cross-sectional images (inset of Figures 1B and S2) show that the CuWO₄ coating is compact along its whole thickness. Therefore, we could estimate the thickness of the photoactive layer in electrodes prepared with 1, 2, 3, and 5 CuWO₄ deposition cycles (Figure 1E).

The phase purity of the CuWO₄ films was assessed through XRD analysis and comparison with the Bragg reflections from JCPDF 72-0616, which revealed a triclinic structure (Figure 1C) and the absence of the WO₃ phase in all electrodes. Although no CuO phase is detectable in the XRD patterns, we washed the electrodes with diluted HCl to dissolve possible CuO impurity traces.

Then, we studied the optical properties of the electrodes by absorption spectroscopy in transmittance mode (Figure 1D). The multilayer films are optically transparent, with the absorbance in the UV region steeply increasing below 450 nm, without obvious absorption peaks consistently with the indirect forbidden d–d transition occurring in this Mott–Hubbard semiconductor,^{35–37} possibly originating light scattering at wavelengths longer than 550 nm.

The main optical transition of CuWO₄ is assigned to the photoexcitation of electrons from the valence band, composed of O 2p states partly mixed with Cu 3d states, to the conduction band—empty Cu 3d levels (inset of Figure 1D).³³ A ca. 2.1 eV energy gap separates the band edges. CuWO₄ has an additional band of empty states at higher energy, i.e., at about 5 eV above the top of the valence band, consisting of W 5d and Cu 3d states. At wavelengths above 550 nm, scattering appears in the

absorption spectrum of thicker films, possibly originating from the bigger grains observed in Figure 1B.

We combined the thickness values obtained from cross-sectional FESEM images and the absorption spectrum of CuWO₄ to estimate the absorption coefficient of CuWO₄ films at 420 nm (the edge between UV and visible light), using the following equation

$$A_{420} = \alpha_{420} \times d$$

where α_{420} (cm⁻¹) is the absorption coefficient of CuWO₄ at 420 nm, A_{420} is the absorption at 420 nm, and d is the average thickness in cm calculated from the cross-sectional FESEM images. From the A_{420} vs film thickness plot (see Figure S3), we calculated the absorption coefficient for CuWO₄ at 420 nm, $\alpha_{420} = (1.65 \pm 0.14) \times 10^4$ cm⁻¹. This value is rather low compared to other semiconductor oxides, consistent with the indirect nature of the CuWO₄ band gap. For instance, it is 4-fold lower than the α_{420} value of BiVO₄ (6.7×10^4 cm⁻¹),³⁸ and this implies that to absorb the same amount of 420 nm photons, a CuWO₄ electrode needs to be 4 times thicker than a BiVO₄ electrode. Interestingly the absorption coefficient for CuWO₄ at 420 nm is also ca. 2-fold lower compared to CuW_{0.5}Mo_{0.5}O₄ (3.41×10^4 cm⁻¹),²⁰ which supports the hypothesis that Mo doping introduces additional optical transitions in CuWO₄.

The α_{420} for CuWO₄ value was then used to evaluate the thickness of the prepared CuWO₄ films from their absorbance at 420 nm. These thickness values are reported in Figure 1E. For convenience, hereafter, we identify the electrodes with different CuWO₄ thicknesses as CuWO₄:X, with X referring to the CuWO₄ thickness in nanometers (rounded to the nearest ten).

We also calculated the extinction coefficient of CuWO₄ at all wavelengths, based on the overall absorption spectrum of the thinnest electrode (which is moderately affected by scattering),

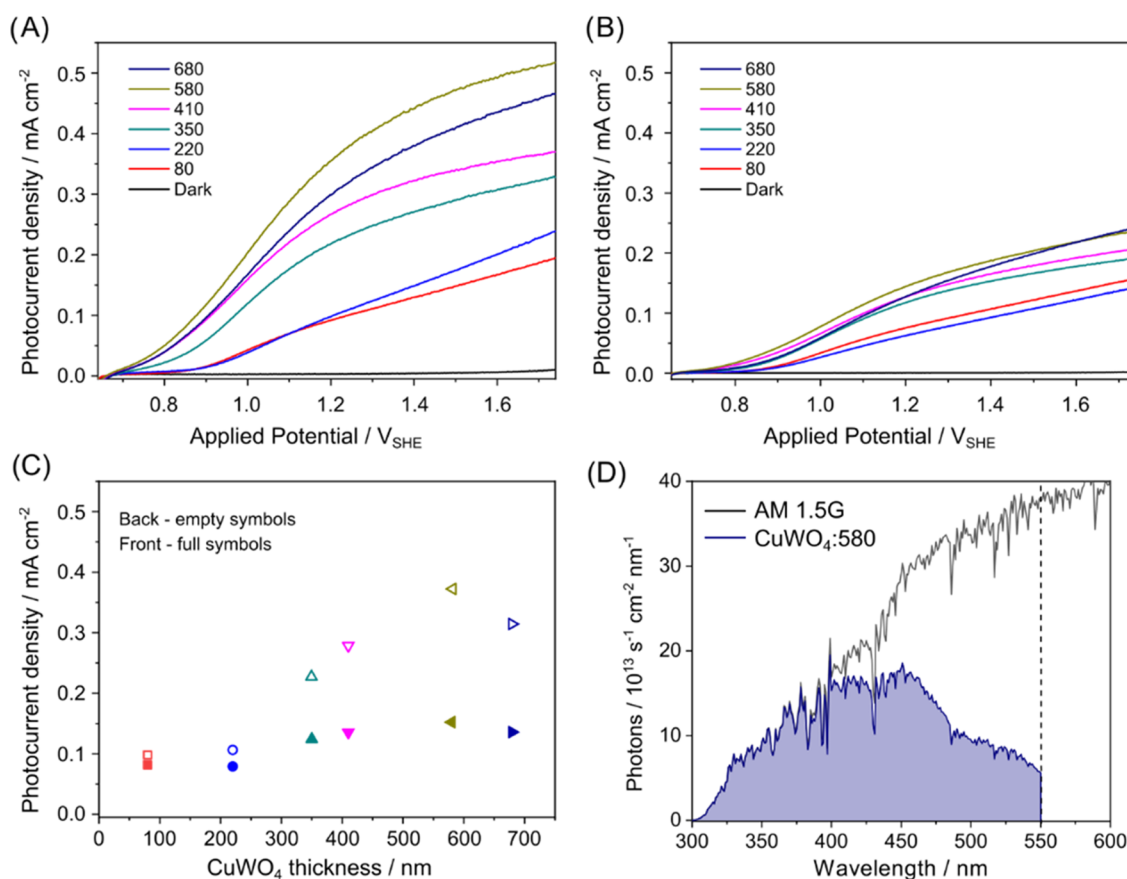


Figure 2. Linear sweep voltammetry (LSV) curves recorded with CuWO_4 multilayer photoanodes under (A) back-side or (B) front-side simulated solar light irradiation (100 mW cm^{-2}) in 0.1 M KBi buffer solution at pH 9. The labels within the figures refer to the thickness of the CuWO_4 layers, in nm. (C) Current density at $1.23 \text{ V}_{\text{SHE}}$ as a function of the CuWO_4 thickness, under back- and front-side irradiation (empty and full symbols, respectively). (D) Overall photon flux in the AM 1.5 solar spectrum (black trace) and number of photons absorbed per second by $\text{CuWO}_4\text{:580}$ (blue area). The dashed vertical line marks the CuWO_4 absorption edge.

as $\alpha_\lambda = \frac{A_\lambda}{d}$, where A_λ is the absorbance over the 300–800 nm interval and d is the film thickness. The so estimated extinction coefficient of CuWO_4 vs wavelength is shown in Figure 1F.

3.2. Photoresponse of CuWO_4 Multilayer Photoanodes. We performed PEC experiments under monochromatic and simulated solar light irradiation to probe the photoresponse of the CuWO_4 electrodes with increasing thickness of the semiconductor layer. The experiments under simulated solar light provide information on their performance under conditions close to field application, while PEC tests performed under monochromatic irradiation provide information on the irradiation wavelength-dependent behavior of photoactive materials. We also tested the electrodes under back-side and front-side irradiation, i.e., with the light reaching CuWO_4 through the FTO or the electrolyte, respectively. Indeed the comparison between the PEC performance in the two modes proved diagnostic for identifying electron or hole transport as a limiting process in the illuminated semiconductor.^{39,40}

Linear sweep voltammetry (LSV) tests performed under simulated solar light irradiation in 0.1 M borate buffer solution (KBi buffer) evidence that the photocurrent vs voltage increases with the CuWO_4 layer thickness (Figure 2A,B), up to a 580 nm thick CuWO_4 photoactive layer. Under back-side irradiation, the electrodes generate a larger photocurrent than under front-side irradiation (Figure 2C). For instance, the photocurrent of the

$\text{CuWO}_4\text{:580}$ electrode under back irradiation is $\geq 2x$ than in the front-side mode.

Indeed, under front-side irradiation, most electrons are photogenerated far from the electron extraction site (the contact with the FTO layer). The lower photocurrent, compared to back-side irradiation, could indicate that electrons in CuWO_4 can travel only short distances because they undergo recombination with photogenerated holes within the film thickness, before reaching the extraction site. With the thinnest $\text{CuWO}_4\text{:80}$ electrode, similar photocurrents are recorded under front- and back-side irradiation (Figure 2A,B), demonstrating that photogenerated electrons can diffuse efficiently at least within a ca. 80 nm distance.

The best-performing $\text{CuWO}_4\text{:580}$ electrode generates a photocurrent density of 0.37 mA cm^{-2} at $1.23 \text{ V}_{\text{SHE}}$ under back-side irradiation. This value is in line with previous records for CuWO_4 -based electrodes prepared with different synthetic strategies (Table 2).^{41,42} However, it is far from the maximum photocurrent expected for the 2.2 eV band gap of CuWO_4 . Indeed, assuming that all absorbed photons in the $\text{CuWO}_4\text{:580}$ electrode (Figure 2D) are completely converted into current would lead to a 5.6 mA cm^{-2} theoretical maximum photoresponse under 1 sun illumination. Thus, the photogenerated current is only 6.7% of this maximum value, which implies that more than 90% of the photogenerated charge carriers undergo recombination.

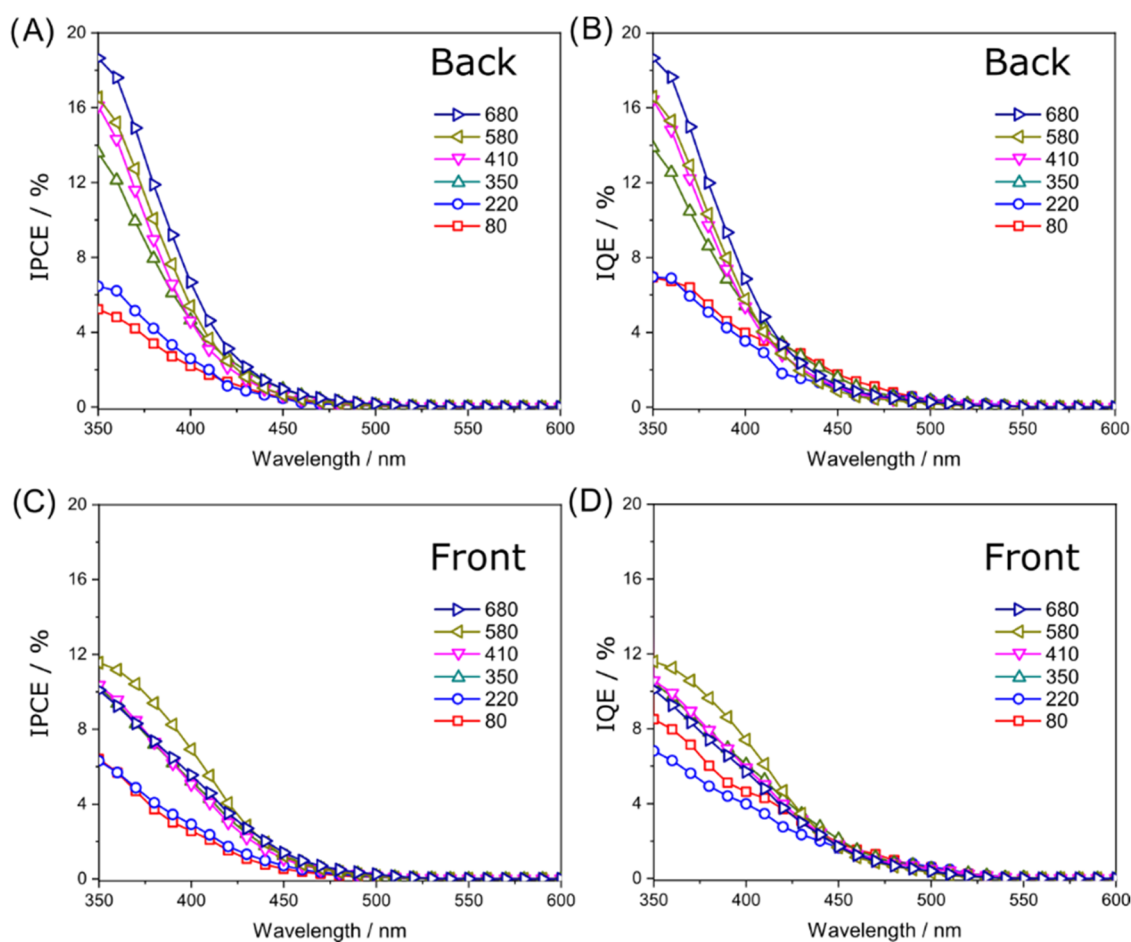


Figure 3. (A, C) IPCE and (B, D) IQE analyses of CuWO_4 multilayer photoanodes under (A, B) back-side and (C, D) front-side monochromatic irradiation, at $1.23 V_{\text{SHE}}$.

Figure 3 shows the incident photon to current efficiency (IPCE) and internal quantum efficiency (IQE) curves recorded with the CuWO_4 photoanodes under back- and front-side irradiation at an applied bias of $1.23 V_{\text{SHE}}$. All IPCE curves monotonously decrease with increasing incident wavelength without any defined peak or steep IPCE feature (Figure 3A,C). This suggests the presence of a single electronic transition with broad rather than sharp band edges within the investigated light energy. The IQE values (Figure 3B,D), which account for the number of absorbed photons which generate photocurrent and is equal to the charge transport efficiency,⁵³ are larger than the IPCE values. However, in this photoelectrode series, the IQE differs slightly from the corresponding IPCE values because of the relatively high electrode absorbance, especially in the UV region where the electrodes completely absorb the incident light. On the other hand, under visible light irradiation, when the electrodes absorb less than 50% of the incident light, the IQE is noticeably larger than the IPCE (Figure S4). The tests performed under monochromatic irradiation with the thickest electrodes pinpoint a CuWO_4 photocurrent onset at ca. 550–560 nm (we measured IPCE at high applied bias, $1.73 V_{\text{SHE}}$) to increase the photocurrent signal close to the band gap excitation edge; see Figures S5 and S6, in good agreement with the reported 2.2–2.3 eV band gap of CuWO_4 .

Under back-side irradiation, the CuWO_4 electrodes generate larger IPCEs than under front-side irradiation, implying that

electron transport issues limit the overall photoresponse of this material and substantiating the behavior observed in LSV tests.³⁹

Notably, under back-side irradiation, in LSV tests CuWO_4 :S80 outperforms the other electrodes (Figure 2A), while in IPCE, the thickest CuWO_4 :680 electrode is best performing (Figure 3A). This difference relies on both the different light intensities (100 mW cm^{-2} in LSV analyses vs a few mW cm^{-2} in IPCE) and the poor electron transport of CuWO_4 . Under back-side irradiation and the low light intensity employed in IPCE analyses, most photons are absorbed close to the FTO glass where electron extraction toward the external circuit easily occurs. However, a larger light intensity (e.g., under simulated solar light irradiation) generates a larger amount of excited electrons deep in the CuWO_4 film, far from FTO, at distances exceeding the mean electron diffusion within CuWO_4 . These electrons are more likely to recombine with holes and limit the overall photocurrent in the thickest electrode.

3.3. Light Intensity Dependence. Employing the best-performing CuWO_4 :S80 photoelectrode, we evaluated the effect on photoactivity of the light intensity under back-side irradiation, to get further information on the charge separation efficiency within the CuWO_4 electrodes. For intensities larger than 1 sun, the measurements were carried out with the electrode in contact with a 0.5 M KBi electrolyte solution because the 0.1 M KBi electrolyte employed in LSV analyses under 1 sun irradiation (Figure 2) was insufficiently conductive

Table 2. Photoelectrochemical Performances of Literature Benchmark CuWO₄ Photoanodes Prepared with Different Synthetic Approaches

synthetic method	electrolyte	thickness/nm	J ^s		stability		ref
			/ mA cm ⁻²	Time / min	J _{fin} ^h / mA cm ⁻²⁻² J _{fin} ^h	J _{fin} ⁱ / mA cm ⁻²⁻² J _{fin} ^h	
spin-coating	0.1 M KPi (pH 7)	580	0.37	120	0.37		this work
one step-hy ^a	0.2 M KPi (pH 7) ^c	~1500	0.38	50	0.3		43
ST - hy ^b	0.1 M KPi (pH 7)	≥1000	~0.3	60	~5% ⁱ		44
ST - hy	0.1 M KPi (pH 7)	≥1000	0.34	240	~35% ⁱ		45
ST - hy	1 M KBi (pH 9) ^f	≥1000	0.4	60	0.39		29
ST - hy	0.1 M KPi (pH 7)	2000	0.42	n/a	n/a		46
ST - hy	0.1 M KPi (pH 7)	≥1000	0.35	240	0.26		47
spin-coating	KPi (pH 7)	500	0.47	600	0.4		48
e-deposition ^c	0.1 M KPi (pH 7)	2–3000	0.18	600	~50% ⁱ		25
ALD ^d	1 M KBi (pH 9.0)	80	~0.15	n/a	n/a		41
ST - hy	0.1 M KPi (pH 7)	≥1000	0.35	60	~17% ⁱ		22
spin coating	0.1 M Na ₂ SO ₄ (pH 6.8)	800	0.27	2.5	0.21		49
spray pyrolysis	0.1 M KPi (pH 7)	1.5–2000	0.19	n/a	n/a		50
spin coating	KPi/NaCl 0.1/0.14 M	250	0.38	n/a	n/a		51
ST - hy	0.1 M KPi (pH 7)	≥1000	0.38	240	0.39		52

^aone-step hydrothermal. ^bsacrificial template–hydrothermal. ^celectrodeposition. ^datomic layer deposition. ^epotassium phosphate buffer. ^fpotassium borate buffer. ^gcurrent density at 1.23 V_{SHE}, ^hcurrent density at 1.23 V_{SHE} at the end of the stability test, ⁱcurrent density percent drop at the end of the stability test (in this case the stability is at a voltage ≥1.23 V_{SHE}).

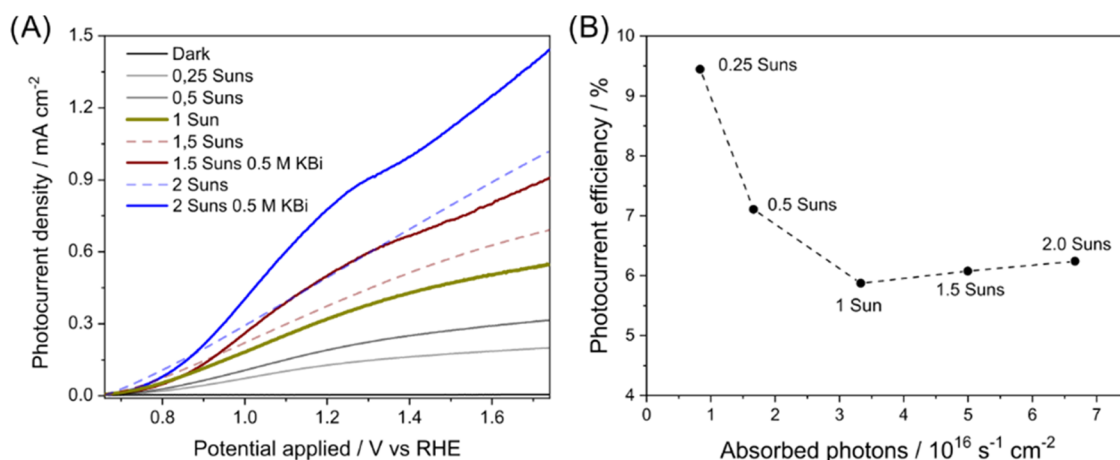


Figure 4. (A) LSV curves recorded with the CuWO₄:580 photoelectrode under different irradiation intensities in contact with 0.1 M (0–1 sun) or 0.5 M (1.5–2 sun) (continuous lines) KBi solutions. The two dashed lines are the LSV curves recorded under 1.5 and 2 sun irradiation in contact with 0.1 M KBi solutions. (B) Photocurrent efficiency at 1.23 V_{SHE} vs absorbed photons per unit time at different irradiation intensities.

to sustain photocurrents larger than 0.5 mA cm⁻² (see dashed lines in Figure 4A).

The photocurrent response of the CuWO₄:580 photoelectrode increases with increasing light intensity (Figure 4A), though this increase is not linear. We thus calculated the absorbed photons to current efficiency (photocurrent efficiency) over the full solar spectrum at different light intensities by dividing the number of photopromoted electrons exiting the CuWO₄ film at 1.23 V_{SHE} by the total number of absorbed photons (Figure 2D, integrated blue area of the absorbed photons per nm). Figure 4B reports the photocurrent efficiency values vs the amount of absorbed photons per unit time.

The photocurrent efficiency decreases with increasing light intensity from 0.25 to 1 sun and stabilizes at ca. 6% for an illumination intensity greater than 1 sun (~3 × 10¹⁶ s⁻¹ cm⁻²). The drop from 0.25 to 1 sun is consistent with an increased charge carrier recombination at high photon flux, as found when comparing IPCE and LSV results, and could be related to inefficient bulk charge extraction at high light intensity.

3.4. Water Oxidation Kinetics of CuWO₄. The PEC characterization of CuWO₄ photoanodes points to a photoactivity up to 550–560 nm and severe charge carrier recombination due to limited electron mobility in the bulk. To collect further information about this weak point of CuWO₄ photoefficiency, we sought to investigate the oxidation reaction and stability of this semiconductor. The results of such an analysis are reported in Figure 5.

We first compared the performance of CuWO₄ to that of an oxide affected by intrinsic sluggish surface water oxidation kinetics. We chose bismuth vanadate because we extensively studied it in previous studies and for its relatively poor photocatalytic activity in the oxygen evolution reaction.⁵⁴ As shown in Figure 5A, the photocurrent response of undoped BiVO₄ at 1.23 V_{SHE} rapidly decreases by more than 60% within a few seconds after the beginning of irradiation. This behavior is usually ascribed to surface hole accumulation due to the slow hole transfer across the semiconductor/electrolyte interface and consequent charge carrier recombination.

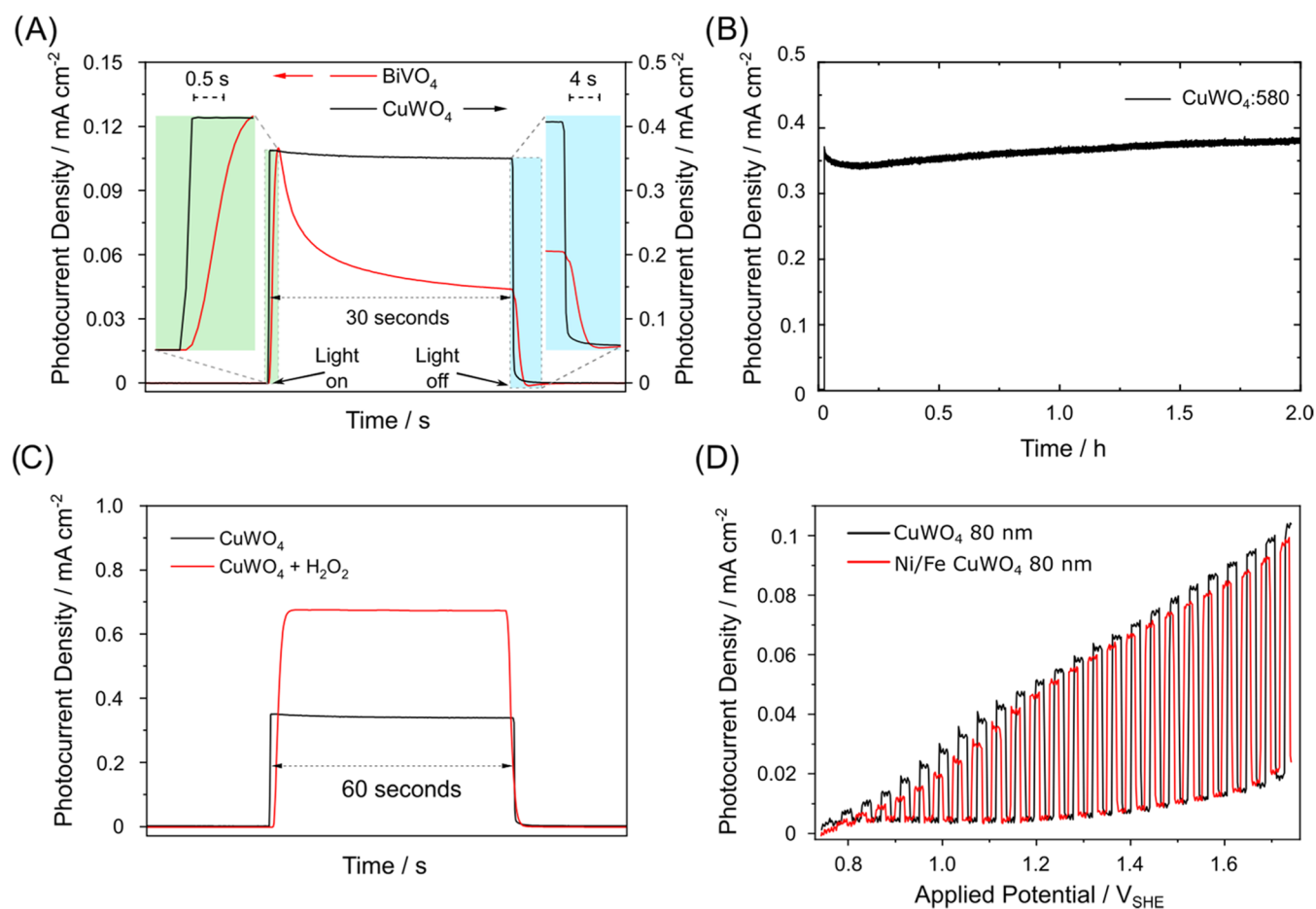


Figure 5. (A) Chopped chronoamperometry under 1 sun irradiation of an 80 nm thick CuWO_4 photoanode (black line) and a 75 nm thick BiVO_4 photoanode (red line), under back-side irradiation at $1.23 V_{\text{SHE}}$. The green (light on) and blue (light off) boxes display expanded portions of the photocurrent curve. (B) Chronoamperometric stability test of the CuWO_4 :580 electrode under simulated solar light irradiation in 0.1 M KBI. (C) Chopped chronoamperometry under 1 sun irradiation of the CuWO_4 :580 photoanode in the presence (red line) or in the absence (black line) of 0.5 M H_2O_2 . (D) Chopped LSV curves recorded with a bare (black line) and Ni/Fe -modified (red line) CuWO_4 :80 photoanode under monochromatic irradiation at 420 nm; the light intensity is 9 mW cm^{-2} .

Moreover, when the light is switched off, a negative capacitive current appears for BiVO_4 due to the consumption of accumulated surface holes via recombination with electrons from the external circuit (a negative current indicates a reductive process taking place at the working electrode). On the other hand, the CuWO_4 photoanode shows a sharp photocurrent onset and negligible photocurrent decrease under irradiation, and a sharp decrease when the light is turned on and off, respectively (Figure 5A). These behaviors point to low hole accumulation at the CuWO_4 surface; that is, consumption of surface holes occurs right after they reach the electrode/electrolyte interface. We also checked the stability of the CuWO_4 electrode and found a negligible activity drop during a 2 h test (see Figure 5B), supporting the low hole accumulation at the surface and the chemical stability of this semiconductor.

To probe the nature of the electron–hole recombination, we performed PEC experiments in the presence of a more feasible oxidation reaction. To do so, we tested the CuWO_4 :580 electrode with an electrolyte containing H_2O_2 as an electron donor. Hydrogen peroxide is much more easily oxidizable than water ($+0.68 V_{\text{SHE}}$ vs $1.23 V_{\text{SHE}}$ for water) and has a higher reaction rate (H_2O_2 to H_2O is a 2-hole process, while H_2O to O_2 is a 4-hole process).²⁴ The current doubled to 0.67 mA cm^{-2} at $1.23 V_{\text{SHE}}$ in the presence of H_2O_2 (Figure 5C). However, this

increase is quite limited compared to BiVO_4 , for which photocurrent increases from a few μA to mA in contact with electron-donor-containing solutions.^{55,56} The moderate photocurrent increase in CuWO_4 suggests that the few holes reaching the photocatalyst surface can very efficiently undergo oxidation reactions (i.e., water or electron donor oxidation). This experimental evidence rules out sluggish surface electron transfer as the main performance bottleneck in these photoactive films and indicates that the low PEC efficiency of CuWO_4 stems far from the surface catalytic sites.

To further check this hypothesis, we deposited a nickel–iron oxyhydroxide water oxidation catalyst on top of CuWO_4 . NiFeO_x ad-layers usually enhance the PEC performance of semiconductors which are limited by poor water oxidation kinetics (e.g., BiVO_4 or Ta_3O_5) or by low chemical stability (Si, or CdTe).^{54,57,58} PEC analyses showed no performance enhancement for the NiFeO_x -modified CuWO_4 photoanode compared to the bare one (Figure 5D). The negligible effect of the NiFeO_x cocatalyst confirms the intrinsic activity of surface CuWO_4 sites and that, therefore, photogenerated charge carriers recombine far from the semiconductor/electrolyte interface.

4. DISCUSSION

The spin coating preparation technique employed here offers a simple way to tune the CuWO₄ thickness and reach a desirable trade-off between visible light absorption and electron–hole separation, resulting in optimal PEC performances. The highest current density achieved (0.37 mA cm⁻² with the 580 nm thick CuWO₄ electrode) aligns with the benchmark literature reports (Table 2). The thickness of the best-performing photoanode (580 nm) is similar to that of transparent electrodes prepared by Tian et al. with a spin-coating synthesis (500 nm),⁴⁸ suggesting that the optimal balance between absorption and charge separation in undoped, bulk, and polycrystalline CuWO₄ is within 5–600 nm. Recently, facet control along the 100 crystal facet showed improved conductivity and enhanced current density (0.38 mA cm⁻²) in bulk 1.5 μm thick CuWO₄ films.⁴³

Nanostructuring provides efficient charge carrier transport.⁵⁹ Indeed, CuWO₄ electrodes with nanoflake morphology^{22,29,44–47,52} facilitate hole extraction from the oxide flakes because their 30–60 nm width is within the hole diffusion length in CuWO₄. However, the film thickness (≥1 μm) exceeds electron diffusion in CuWO₄ and likely limits the PEC performance to ~0.4 mA cm⁻².

Doping and mild reduction via hydrogenation of semiconductors offer further control of the defectivity and charge carrier density. For example, Mo doping in BiVO₄ improves PEC performances by increasing electron mobility, disfavoring recombination, and enhancing charge separation.^{60,61} These strategies induce similar chemical and electronic effects in CuWO₄ and translate into efficiency improvements (from 0.30 to 0.39 mA cm⁻² for hydrogenation,⁴⁴ from 0.35 to 0.62 mA cm⁻² for Mo doping,²² from 0.27 to 0.42 mA cm⁻² for Fe doping,^{49,50} from 0.38 to 0.57 mA cm⁻² for fluorine doping).⁵²

The moderate photocurrent increase observed with CuWO₄ in the presence of hole scavengers such as H₂O₂ (Figure 5C) indicates that few holes reach the electrode/electrolyte interface, where they are rapidly consumed at surface catalytic sites.⁴¹ This could be behind the slight photocurrent increase reported in previous work with Co-based oxygen evolution cocatalysts (from 0.34 to 0.42 mA cm⁻² with CoPi,⁴⁵ from 0.32 to 0.54 with CoIrO_x⁴⁷ and from 0.4 to 0.5 mA cm⁻² with Co₃O₄).⁴⁸ In this work, we observed that the PEC performance of CuWO₄ photoanodes is unmodified after coating them with NiFeO_x. The lack of change in photoactivity could rely on the ineffective junction between the two materials. These findings further support the fact that Co-based oxygen evolution catalysts are more suitable to enhance the activity of CuWO₄ than Ni- and Fe-based ones. The simple synthesis reported here could offer a good platform to further enhance the CuWO₄ performance via these synthetic and postsynthetic approaches.

5. CONCLUSIONS

CuWO₄ photoanodes are good candidates for PEC water splitting applications. In fact, CuWO₄ is very photostable and, compared with other semiconductor oxides, has a high intrinsic activity of the surface catalytic sites for water oxidation. On the other hand, PEC tests under front- and back-side irradiation confirm the low mobility of photoelectrons in CuWO₄ and indicate that more than 90% of photogenerated charge carriers recombine in the bulk, which heavily limits the photon to current efficiency of CuWO₄. The higher quantum efficiencies at low light intensities (e.g., IPCE or below 1 sun) indicate that charge separation becomes less efficient at high photogenerated

charge carrier densities and that charge recombination occurs mainly in bulk at defects or interface states. Therefore, CuWO₄ electrode optimization requires reducing this internal charge recombination through: (i) nanostructuring, to facilitate electron extraction toward FTO; (ii) defect engineering, to minimize the presence of recombination centers; and (iii) doping the crystalline structure, to act on the electronic states of the material and modulate its charge transport properties.

■ ASSOCIATED CONTENT

Supporting Information

The Supporting Information is available free of charge at <https://pubs.acs.org/doi/10.1021/acsaem.3c01608>.

Field emission electron microscopy images, absorbance vs thickness plot, IPCE and IQE plot for the CuWO₄-350 electrode, IPCE at 1.73 V_{SHE} (PDF)

■ AUTHOR INFORMATION

Corresponding Author

Ivan Grigioni – Dipartimento di Chimica, Università degli Studi di Milano, 20133 Milano, Italy; orcid.org/0000-0002-9469-4570; Email: ivan.grigioni@unimi.it

Authors

Annalisa Polo – Dipartimento di Chimica, Università degli Studi di Milano, 20133 Milano, Italy; orcid.org/0000-0001-5724-2607

Chiara Nomellini – Dipartimento di Chimica, Università degli Studi di Milano, 20133 Milano, Italy

Laura Vigni – Dipartimento di Chimica, Università degli Studi di Milano, 20133 Milano, Italy

Alessandro Poma – Dipartimento di Chimica, Università degli Studi di Milano, 20133 Milano, Italy

Maria Vittoria Dozzi – Dipartimento di Chimica, Università degli Studi di Milano, 20133 Milano, Italy; orcid.org/0000-0002-6390-9348

Elena Selli – Dipartimento di Chimica, Università degli Studi di Milano, 20133 Milano, Italy; orcid.org/0000-0001-8391-7639

Complete contact information is available at: <https://pubs.acs.org/doi/10.1021/acsaem.3c01608>

Notes

The authors declare no competing financial interest.

■ ACKNOWLEDGMENTS

This work was supported by the Cariplo Foundation through the Project 2021-0664 entitled “Carbon dioxide conversion into energy-rich molecules with tailored catalysts” (CO2EnRich). I.G. acknowledges the European Union’s Horizon 2020 research and innovation programme under Marie Skłodowska-Curie grant (agreement no. 846107).

■ REFERENCES

- (1) Hisatomi, T.; Kubota, J.; Domen, K. Recent Advances in Semiconductors for Photocatalytic and Photoelectrochemical Water Splitting. *Chem. Soc. Rev.* **2014**, *43*, 7520–7535.
- (2) Bard, A. J.; Fox, M. A. Artificial Photosynthesis: Solar Splitting of Water to Hydrogen and Oxygen. *Acc. Chem. Res.* **1995**, *28*, 141–145.
- (3) Cowan, A. J.; Barnett, C. J.; Pendlebury, S. R.; Barroso, M.; Sivula, K.; Grätzel, M.; Durrant, J. R.; Klug, D. R. Activation Energies for the Rate-Limiting Step in Water Photooxidation by Nanostructured α-Fe₂O₃ Nd TiO₂. *J. Am. Chem. Soc.* **2011**, *133*, 10134–10140.

- (4) Alexander, B. D.; Kulesza, P. J.; Rutkowska, I.; Solarska, R.; Augustynski, J. Metal Oxide Photoanodes for Solar Hydrogen Production. *J. Mater. Chem.* **2008**, *18*, 2298–2303.
- (5) Tilley, S. D.; Cornuz, M.; Sivula, K.; Grätzel, M. Light-Induced Water Splitting with Hematite: Improved Nanostructure and Iridium Oxide Catalysis. *Angew. Chem., Int. Ed.* **2010**, *49*, 6405–6408.
- (6) Wang, H.; Lindgren, T.; He, J.; Hagfeldt, A.; Lindquist, S. E. Photoelectrochemistry of Nanostructured WO_3 Thin Film Electrodes for Water Oxidation: Mechanism of Electron Transport. *J. Phys. Chem. B* **2000**, *104*, 5686–5696.
- (7) Reyes-Gil, K. R.; Brunchwitz, B. S.; Lewis, N. S. Comparison between the Quantum Yields of Compact and Porous WO_3 Photoanodes. *J. Phys. Chem. C* **2013**, *117*, 14947–14957.
- (8) Li, H.; Lin, C.; Yang, Y.; Dong, C.; Min, Y.; Shi, X.; Wang, L.; Lu, S.; Zhang, K. Boosting Reactive Oxygen Species Generation Using Inter-Facet Edge Rich WO_3 Arrays for Photoelectrochemical Conversion. *Angew. Chem., Int. Ed.* **2023**, *62*, No. e202210804, DOI: 10.1002/anie.202210804.
- (9) Prévot, M. S.; Sivula, K. Photoelectrochemical Tandem Cells for Solar Water Splitting. *J. Phys. Chem. C* **2013**, *117*, 17879–17893.
- (10) Huang, Z.; Lin, Y.; Xiang, X.; Rodríguez-Córdoba, W.; McDonald, K. J.; Hagen, K. S.; Choi, K.-S.; Brunchwitz, B. S.; Musaev, D. G.; Hill, C. L.; Wang, D.; Lian, T. In Situ Probe of Photocarrier Dynamics in Water-Splitting Hematite ($\alpha\text{-Fe}_2\text{O}_3$) Electrodes. *Energy Environ. Sci.* **2012**, *5*, 8923.
- (11) Cherepy, N. J.; Liston, D. B.; Lovejoy, J. A.; Deng, H.; Zhang, J. Z. Ultrafast Studies of Photoexcited Electron Dynamics in γ - and $r\text{-Fe}_2\text{O}_3$ Semiconductor Nanoparticles. *J. Phys. Chem. B* **1998**, *5647*, 770–776, DOI: 10.1021/jp973149e.
- (12) Kim, T. W.; Choi, K. S. Nanoporous BiVO_4 Photoanodes with Dual-Layer Oxygen Evolution Catalysts for Solar Water Splitting. *Science* **2014**, *343*, 990–994.
- (13) Park, Y.; McDonald, K. J.; Choi, K. S. Progress in Bismuth Vanadate Photoanodes for Use in Solar Water Oxidation. *Chem. Soc. Rev.* **2013**, *42*, 2321–2337.
- (14) Polo, A.; Lhermitte, C. R.; Dozzi, M. V.; Selli, E.; Sivula, K. Hydrogenation of ZnFe_2O_4 Flat Films: Effects of the Pre-Annealing Temperature on the Photoanodes Efficiency for Water Oxidation. *Surfaces* **2020**, *3*, 93–104.
- (15) Lee, D. K.; Lee, D.; Lumley, M. A.; Choi, K. S. Progress on Ternary Oxide-Based Photoanodes for Use in Photoelectrochemical Cells for Solar Water Splitting. *Chem. Soc. Rev.* **2019**, *48*, 2126–2157.
- (16) Lin, C.; Dong, C.; Kim, S.; Lu, Y.; Wang, Y.; Yu, Z.; Gu, Y.; Gu, Z.; Lee, D. K.; Zhang, K.; Park, J. H. Photo-Electrochemical Glycerol Conversion over a Mie Scattering Effect Enhanced Porous BiVO_4 Photoanode. *Adv. Mater.* **2023**, *35*, No. 2209955, DOI: 10.1002/adma.202209955.
- (17) Pihosh, Y.; Turkevych, I.; Mawatari, K.; Uemura, J.; Kazoe, Y.; Kosar, S.; Makita, K.; Sugaya, T.; Matsui, T.; Fujita, D.; Tosa, M.; Kondo, M.; Kitamori, T. Photocatalytic Generation of Hydrogen by Core-Shell $\text{WO}_3/\text{BiVO}_4$ Nanorods with Ultimate Water Splitting Efficiency. *Sci. Rep.* **2015**, *5*, No. 11141.
- (18) Kim, J. H.; Jang, J. W.; Jo, Y. H.; Abdi, F. F.; Lee, Y. H.; Van De Krol, R.; Lee, J. S. Hetero-Type Dual Photoanodes for Unbiased Solar Water Splitting with Extended Light Harvesting. *Nat. Commun.* **2016**, *7*, No. 13380.
- (19) Gaillard, N.; Chang, Y.; Deangelis, A.; Higgins, S.; Braun, A. A Nanocomposite Photoelectrode Made of 2.2 eV Band Gap Copper Tungstate (CuWO_4) and Multi-Wall Carbon Nanotubes for Solar-Assisted Water Splitting. *Int. J. Hydrogen Energy* **2013**, *38*, 3166–3176.
- (20) Polo, A.; Nomellini, C.; Grigioni, I.; Dozzi, M. V.; Selli, E. Effective Visible Light Exploitation by Copper Molybdo-Tungstate Photoanodes. *ACS Appl. Energy Mater.* **2020**, *3*, 6956–6964.
- (21) Hill, J. C.; Ping, Y.; Galli, G. A.; Choi, K. S. Synthesis, Photoelectrochemical Properties, and First Principles Study of n-Type $\text{CuW}_{1-x}\text{Mo}_x\text{O}_4$ Electrodes Showing Enhanced Visible Light Absorption. *Energy Environ. Sci.* **2013**, *6*, 2440–2446.
- (22) Yang, J.; Li, C.; Diao, P. Molybdenum Doped CuWO_4 Nanoflake Array Films as an Efficient Photoanode for Solar Water Splitting. *Electrochim. Acta* **2019**, *308*, 195–205.
- (23) Lhermitte, C. R.; Bartlett, B. M. Advancing the Chemistry of CuWO_4 for Photoelectrochemical Water Oxidation. *Acc. Chem. Res.* **2016**, *49*, 1121–1129.
- (24) Uemura, Y.; Ismail, A. S. M.; Park, S. H.; Kwon, S.; Kim, M.; Niwa, Y.; Wadati, H.; Elnaggar, H.; Frati, F.; Haarman, T.; Höppel, N.; Huse, N.; Hirata, Y.; Zhang, Y.; Yamagami, K.; Yamamoto, S.; Matsuda, I.; Katayama, T.; Togashi, T.; Owada, S.; Yabashi, M.; Halisdemir, U.; Koster, G.; Yokoyama, T.; Weckhuysen, B. M.; De Groot, F. M. F. Femtosecond Charge Density Modulations in Photoexcited CuWO_4 . *J. Phys. Chem. C* **2021**, *125*, 7329–7336.
- (25) Yourey, J. E.; Bartlett, B. M. Electrochemical Deposition and Photoelectrochemistry of CuWO_4 , a Promising Photoanode for Water Oxidation. *J. Mater. Chem.* **2011**, *21*, 7651–7660.
- (26) Grigioni, I.; Abdellah, M.; Corti, A.; Dozzi, M. V.; Hammarström, L.; Selli, E. Photoinduced Charge-Transfer Dynamics in $\text{WO}_3/\text{BiVO}_4$ Photoanodes Probed through Midinfrared Transient Absorption Spectroscopy. *J. Am. Chem. Soc.* **2018**, *140*, 14042–14045.
- (27) Selim, S.; Francàs, L.; García-Tecedor, M.; Corby, S.; Blackman, C.; Gimenez, S.; Durrant, J. R.; Kafizas, A. $\text{WO}_3/\text{BiVO}_4$: Impact of Charge Separation at the Timescale of Water Oxidation. *Chem. Sci.* **2019**, *10*, 2643–2652.
- (28) Pili, S. K.; Deutsch, T. G.; Furtak, T. E.; Brown, L. D.; Turner, J. A.; Herring, A. M. $\text{BiVO}_4/\text{CuWO}_4$ Heterojunction Photoanodes for Efficient Solar Driven Water Oxidation. *Phys. Chem. Chem. Phys.* **2013**, *15*, 3273–3278.
- (29) Ye, W.; Chen, F.; Zhao, F.; Han, N.; Li, Y. CuWO_4 Nanoflake Array-Based Single-Junction and Heterojunction Photoanodes for Photoelectrochemical Water Oxidation. *ACS Appl. Mater. Interfaces* **2016**, *8*, 9211–9217.
- (30) Grigioni, I.; Corti, A.; Dozzi, M. V.; Selli, E. Photoactivity and Stability of $\text{WO}_3/\text{BiVO}_4$ Photoanodes: Effects of the Contact Electrolyte and of Ni/Fe Oxyhydroxide Protection. *J. Phys. Chem. C* **2018**, *122*, 13969–13978.
- (31) Selim, S.; Francàs, L.; García-Tecedor, M.; Corby, S.; Blackman, C.; Gimenez, S.; Durrant, J. R.; Kafizas, A. $\text{WO}_3/\text{BiVO}_4$: Impact of Charge Separation at the Timescale of Water Oxidation. *Chem. Sci.* **2019**, *10*, 2643–2652.
- (32) Grigioni, I.; Dozzi, M. V.; Selli, E. Photoinduced Electron Transfer in $\text{WO}_3/\text{BiVO}_4$ Heterojunction Photoanodes: Effects of the WO_3 Layer Thickness. *J. Phys.: Condens. Matter* **2020**, *32*, No. 014001.
- (33) Grigioni, I.; Polo, A.; Dozzi, M. V.; Ganzer, L.; Bozzini, B.; Cerullo, G.; Selli, E. Ultrafast Charge Carrier Dynamics in CuWO_4 Photoanodes. *J. Phys. Chem. C* **2021**, *125*, 5692–5699.
- (34) Cai, L.; Zhao, J.; Li, H.; Park, J.; Cho, I. S.; Han, H. S.; Zheng, X. One-Step Hydrothermal Deposition of Ni:FeOOH onto Photoanodes for Enhanced Water Oxidation. *ACS Energy Lett.* **2016**, *1*, 624–632.
- (35) Thang, H. V.; Albanese, E.; Pacchioni, G. Electronic Structure of CuWO_4 : Dielectric-Dependent, Self-Consistent Hybrid Functional Study of a Mott-Hubbard Type Insulator. *J. Phys.: Condens. Matter* **2019**, *31*, No. 145503, DOI: 10.1088/1361-648X/aaff3e.
- (36) Sorenson, S.; Driscoll, E.; Haghigat, S.; Dawlaty, J. M. Ultrafast Carrier Dynamics in Hematite Films: The Role of Photoexcited Electrons in the Transient Optical Response. *J. Phys. Chem. C* **2014**, *118*, 23621–23626.
- (37) Dey, S.; Ricciardo, R. A.; Cuthbert, H. L.; Woodward, P. M. Metal-to-Metal Charge Transfer in AWO_4 ($A = \text{Mg, Mn, Co, Ni, Cu, or Zn}$) Compounds with the Wolframite Structure. *Inorg. Chem.* **2014**, *53*, 4394–4399.
- (38) Grigioni, I.; Polo, A.; Dozzi, M. V.; Stamplescok, K. G.; Jara, D. H.; Kamat, P. V.; Selli, E. Enhanced Charge Carrier Separation in $\text{WO}_3/\text{BiVO}_4$ Photoanodes Achieved via Light Absorption in the BiVO_4 Layer. *ACS Appl. Energy Mater.* **2022**, *5*, 13142–13148.
- (39) Liang, Y.; Tsubota, T.; Mooij, L. P. A.; Van De Krol, R. Highly Improved Quantum Efficiencies for Thin Film BiVO_4 Photoanodes. *J. Phys. Chem. C* **2011**, *115*, 17594–17598.

- (40) Abdi, F. F.; Van De Krol, R. Nature and Light Dependence of Bulk Recombination in Co-Pi-Catalyzed BiVO₄ Photoanodes. *J. Phys. Chem. C* **2012**, *116*, 9398–9404.
- (41) Gao, Y.; Hamann, T. W. Quantitative Hole Collection for Photoelectrochemical Water Oxidation with CuWO₄. *Chem. Commun.* **2017**, *53*, 1285–1288.
- (42) Shadabipour, P.; Raithel, A. L.; Hamann, T. W. Charge-Carrier Dynamics at the CuWO₄/Electrocatalyst Interface for Photoelectrochemical Water Oxidation. *ACS Appl. Mater. Interfaces* **2020**, *12*, 50592–50599.
- (43) Chen, L.; Li, W.; Qiu, W.; He, G.; Wang, K.; Liu, Y.; Wu, Q.; Li, J. Oriented CuWO₄ Films for Improved Photoelectrochemical Water Splitting. *ACS Appl. Mater. Interfaces* **2022**, *14*, 47737–47746.
- (44) Hu, D.; Diao, P.; Xu, D.; Xia, M.; Gu, Y.; Wu, Q.; Li, C.; Yang, S. Copper(II) Tungstate Nanoflake Array Films: Sacrificial Template Synthesis, Hydrogen Treatment, and Their Application as Photoanodes in Solar Water Splitting. *Nanoscale* **2016**, *8*, 5892–5901.
- (45) Li, C.; Guo, B.; Peng, B.; Yue, C.; Diao, P. Copper Tungstate (CuWO₄) Nanoflakes Coupled with Cobalt Phosphate (Co-Pi) for Effective Photoelectrochemical Water Splitting. *Int. J. Electrochem. Sci.* **2019**, *14*, 9017–9029.
- (46) Liu, Z.; Song, Q.; Zhou, M.; Guo, Z.; Kang, J.; Yan, H. Synergistic Enhancement of Charge Management and Surface Reaction Kinetics by Spatially Separated Cocatalysts and p-n Heterojunctions in Pt/CuWO₄/Co₃O₄ Photoanode. *Chem. Eng. J.* **2019**, *374*, 554–563.
- (47) Li, C.; Diao, P. Boosting the Activity and Stability of Copper Tungsten Nanoflakes toward Solar Water Oxidation by Iridium-Cobalt Phosphates Modification. *Catalysts* **2020**, *10*, No. 913, DOI: [10.3390/catal10080913](https://doi.org/10.3390/catal10080913).
- (48) Tian, C. M.; Jiang, M.; Tang, D.; Qiao, L.; Xiao, H. Y.; Oropeza, F. E.; Hofmann, J. P.; Hensen, E. J. M.; Tadich, A.; Li, W.; Qi, D. C.; Zhang, K. H. L. Elucidating the Electronic Structure of CuWO₄ Thin Films for Enhanced Photoelectrochemical Water Splitting. *J. Mater. Chem. A* **2019**, *7*, 11895–11907.
- (49) Sun, Y.; Du, F.; Xie, D.; Yang, D.; Jiao, Y.; Jia, L.; Fan, H. Improved Water Oxidation via Fe Doping of CuWO₄ Photoanodes: Influence of the Fe Source and Concentration. *Chin. Phys. B* **2020**, *29*, No. 127801, DOI: [10.1088/1674-1056/aba9cb/meta](https://doi.org/10.1088/1674-1056/aba9cb/meta).
- (50) Bohra, D.; Smith, W. A. Improved Charge Separation via Fe-Doping of Copper Tungstate Photoanodes. *Phys. Chem. Chem. Phys.* **2015**, *17*, 9857–9866.
- (51) Zhang, H.; Yilmaz, P.; Ansari, J. O.; Khan, F. F.; Binions, R.; Krause, S.; Dunn, S. Incorporation of Ag Nanowires in CuWO₄ for Improved Visible Light-Induced Photoanode Performance. *J. Mater. Chem. A* **2015**, *3*, 9638–9644.
- (52) Li, C.; Diao, P. Fluorine Doped Copper Tungsten Nanoflakes with Enhanced Charge Separation for Efficient Photoelectrochemical Water Oxidation. *Electrochim. Acta* **2020**, *352*, No. 136471.
- (53) Nair, V.; Perkins, C. L.; Lin, Q.; Law, M. Textured Nanoporous Mo:BiVO₄ Photoanodes with High Charge Transport and Charge Transfer Quantum Efficiencies for Oxygen Evolution. *Energy Environ. Sci.* **2016**, *9*, 1412–1429.
- (54) Seabold, J. A.; Choi, K. S. Efficient and Stable Photo-Oxidation of Water by a Bismuth Vanadate Photoanode Coupled with an Iron Oxyhydroxide Oxygen Evolution Catalyst. *J. Am. Chem. Soc.* **2012**, *134*, 2186–2192.
- (55) Polo, A.; Grigioni, I.; Magni, M.; Facibeni, A.; Dozzi, M. V.; Selli, E. Unravelling the Bulk and Interfacial Charge Transfer Effects of Molybdenum Doping in BiVO₄ Photoanodes. *Appl. Surf. Sci.* **2021**, *556*, No. 149759.
- (56) Grigioni, I.; Stamplescokie, K. G.; Selli, E.; Kamat, P. V. Dynamics of Photogenerated Charge Carriers in WO₃/BiVO₄ Heterojunction Photoanodes. *J. Phys. Chem. C* **2015**, *119*, 20792–20800.
- (57) Zhao, J.; Cai, L.; Li, H.; Shi, X.; Zheng, X. Stabilizing Silicon Photocathodes by Solution-Deposited Ni-Fe Layered Double Hydroxide for Efficient Hydrogen Evolution in Alkaline Media. *ACS Energy Lett.* **2017**, *2*, 1939–1946.
- (58) Higashi, T.; Nishiyama, H.; Suzuki, Y.; Sasaki, Y.; Hisatomi, T.; Katayama, M.; Minegishi, T.; Seki, K.; Yamada, T.; Domen, K. Transparent Ta₃N₅ Photoanodes for Efficient Oxygen Evolution toward the Development of Tandem Cells. *Angew. Chem., Int. Ed.* **2019**, *58* (8), 2300–2304.
- (59) Su, J.; Feng, X.; Sloppy, J. D.; Guo, L.; Grimes, C. A. Vertically Aligned WO₃ Nanowire Arrays Grown Directly on Transparent Conducting Oxide Coated Glass: Synthesis and Photoelectrochemical Properties. *Nano Lett.* **2011**, *11*, 203–208.
- (60) Polo, A.; Dozzi, M. V.; Grigioni, I.; Lhermitte, C.; Plainpan, N.; Moretti, L.; Cerullo, G.; Sivula, K.; Selli, E. Multiple Effects Induced by Mo⁶⁺ Doping in BiVO₄ Photoanodes. *Sol. RRL* **2022**, No. 2200349, DOI: [10.1002/solr.202200349](https://doi.org/10.1002/solr.202200349).
- (61) Ding, K.; Chen, B.; Fang, Z.; Zhang, Y.; Chen, Z. Why the Photocatalytic Activity of Mo-Doped BiVO₄ Is Enhanced: A Comprehensive Density Functional Study. *Phys. Chem. Chem. Phys.* **2014**, *16*, 13465–13476.